

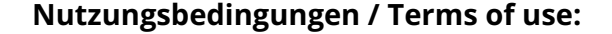


Bifunctional labeling of rabbit mesenchymal stem cells for MR imaging and fluorescence microscopy

Markus T. Berninger, Pablo Rodriguez-Gonzalez, Franz Schilling, Bernhard Haller, Thorsten Lichtenstein, Andreas B. Imhoff, Ernst J. Rummeny, Martina Anton, Stephan Vogt, Tobias D. Henning

Angaben zur Veröffentlichung / Publication details:

Berninger, Markus T., Pablo Rodriguez-Gonzalez, Franz Schilling, Bernhard Haller, Thorsten Lichtenstein, Andreas B. Imhoff, Ernst J. Rummeny, Martina Anton, Stephan Vogt, and Tobias D. Henning. 2020. "Bifunctional labeling of rabbit mesenchymal stem cells for MR imaging and fluorescence microscopy." *Molecular Imaging and Biology* 22 (2): 303–12. https://doi.org/10.1007/s11307-019-01385-8.



Bifunctional Labeling of Rabbit Mesenchymal Stem Cells for MR Imaging and Fluorescence Microscopy

Markus T. Berninger, ^{1,2} Pablo Rodriguez-Gonzalez, Franz Schilling, Bernhard Haller, Thorsten Lichtenstein, Andreas B. Imhoff, Ernst J. Rummeny, Martina Anton, Stephan Vogt, Tobias D. Henning, Henning,

Abstract

Purpose: Longitudinal imaging studies are important in the translational process of stem cellbased therapies. Small animal imaging models are widely available and practical but insufficiently depict important morphologic detail. In contrary, large animal models are logistically challenging and costly but offer greater imaging quality. In order to combine the advantages of both, we developed an intermediate-sized rabbit animal model for cartilage imaging studies. Procedures: Rabbit mesenchymal stem cells (rMSC) were isolated as primary cultures from the bone marrow of New Zealand white rabbits. rMSC were subsequentially transduced lentivirally with eGFP and magnetically labeled with the iron oxide ferucarbotran. eGFP expression was evaluated by flow cytometry and iron uptake was analyzed by isotope dilution mass spectrometry and Prussian blue staining. Fluorescence microscopy of eGFP-transduced rMSC was performed. Viability and induction of apoptosis were assessed by XTT and caspase-3/-7 measurements. The chondrogenic potential of labeled cells was quantified by glycosaminoglycan contents in TGF-β3 induced pellet cultures. Labeled and unlabeled cells underwent magnetic resonance imaging (MRI) at 1.5 T before and after differentiation using T1-, T2-, and T2*-weighted pulse sequences. Relaxation rates were calculated. rMSCs were implanted in fibrin clots in osteochondral defects of cadaveric rabbit knees and imaged by 7 T MRI. T2* maps were calculated. Statistical analyses were performed using multiple regression models.

¹Department of Orthopaedic Sports Medicine, Klinikum rechts der Isar, Technische Universität München, Munich, Germany

²Department of Trauma Surgery, BG Trauma Center Murnau, Prof.-Küntscher-Strasse 8, 82418, Murnau, Germany

³Department of Physical and Analytical Chemistry, University of Oviedo, Oviedo, Spain

⁴Department of Nuclear Medicine, Klinikum rechts der Isar, Technische Universität München, Munich, Germany

⁵Institute for Medical Statistics and Epidemiology, Klinikum rechts der Isar, Technische Universität München, Munich, Germany

⁶Section of Neuroradiology, Uniklinik Köln, Cologne, Germany

⁷Department of Radiology, Klinikum rechts der Isar, Technische Universität München, Munich, Germany

⁸Institute for Experimental Oncology and Therapy Research, Klinikum rechts der Isar, Technische Universität München, Munich, Germany

⁹Section of Neuroradiology, Krankenhaus der Barmherzigen Brüder, Trier, Germany

Results: Efficiency of lentiviral transduction was greater than 90 %. Fluorescence signal was dose dependent. Cellular iron uptake was significant for all concentrations (p<0.05) and dose dependent (3.3–56.5 pg Fe/cell). Labeled rMSC showed a strong, dose-dependent contrast on all MR pulse sequences and a significant decrease in T2 and T2* relaxation rates. Compared with non-transduced or unlabeled controls, there were no adverse effects on cell viability, rate of apoptosis, or chondrogenic differentiation. MRI of labeled rMSCs in osteochondral defects showed a significant signal of the transplant with additional high-resolution anatomical information.

Conclusions: This intermediate-sized rabbit model and its bifunctional labeling technique allow for improved depiction of anatomic detail for noninvasive *in vivo* rMSC tracking with MRI and for immunohistological correlation by fluorescence microscopy.

Key words: Mesenchymal stem cells, Rabbit, MR imaging, Fluorescence microscopy, Bifunctional labeling, Ferucarbotran, eGFP, Chondrogenic differentiation, Osteochondral defects

Introduction

In recent years, the use of mesenchymal stem cells (MSC) has emerged as a promising alternative for the treatment of various diseases like myocardial infarction [1, 2], diabetes [3, 4], or cartilage diseases [5–7]. In the context of cartilage repair, MSC were shown to have several major advantages as compared with chondrocytes, which are already in clinical use [8-10]. However, the exact processes that take place at a molecular and biochemical level after implantation of MSC in diseased joints are not fully understood yet. It was shown that implanted MSC only partially undergo chondrogenesis, while many implanted cells migrated to other parts of the joint in order to stimulate the cartilage formation by trophic, anti-inflammatory, and immunosuppressive activity [11, 12]. In addition, MSC appeared to alter the local microenvironment and stimulate endogenous progenitor cells to develop regenerative activity [10, 13].

To illustrate these intraarticular processes, a noninvasive longitudinal imaging method of the implanted cells is desirable. This could help to track cell migration in experimental models and to detect a possible treatment failure early on. Cellular magnetic resonance imaging (MRI) is a promising technique for this purpose [12, 14, 15]. Compared with other imaging modalities for cell tracking as, e.g., optical imaging or positron emission tomography/x-ray computed tomography, MRI has the advantage of a high anatomical resolution (<1 mm) and superior soft tissue contrast without radiation exposure [16, 17]. In order to detect and track implanted MSC via MR imaging, cells must be labeled with a contrast agent.

For this purpose, numerous labeling techniques have been proposed, mainly using superparamagnetic iron oxide particles (SPIO) [18, 19] or ultrasmall SPIO (USPIO) [20, 21]. Iron oxide contrast agents show high MR sensitivity, good biocompatibility [19], and long-term stable MR contrast effects [22]. Ferucarbotran (Resovist®) is a SPIO, which was approved for clinical application in Europe [23]. It is advantageous over other iron-based contrast agents for its higher labeling efficiency [24,

25] and without toxic side effects at appropriate concentrations [26]. Several studies have shown that human MSC can be efficiently labeled with ferucarbotran without the need of a transfection agent [22, 27].

For practical and economic reasons, experimental studies have mainly been conducted in small animal models (*e.g.*, mouse, rat) [28, 29]. However, due to the small size, these models often do not sufficiently depict anatomical and pathological detail or treatment effects even when used in dedicated small animal scanners. Furthermore, surgical interventions in such models are difficult to perform and less precise. In contrary, larger animal models (*e.g.*, pig, goat) exist [30, 31] and show these details [29, 32], but they require considerable logistic and financial effort and thus have only been used infrequently in the past.

Thus, the purpose of this study was to combine advantages of small and large animal models, *e.g.*, to develop an appropriate intermediate-sized animal model in rabbits, that would enable for precise surgery, high-resolution imaging while being financially and logistically affordable. More specifically, our goal was to (a) create primary cultures of rabbit MSC (rMSC), (b) to design a labeling protocol, and (c) to offer proof of principle imaging data.

Material and Methods

The "Material and Methods" section is provided in detail in the Electronic Supplementary Material (ESM).

Results

eGFP Transduction

The transient production of eGFP expressing lentivirus resulted in a titer of 6×10^9 ($\pm 0.6 \times 10^9$) virus particles (VP)/ml. The lentiviral transduction of rMSC with dilution series of this stock solution resulted in a dose-dependent increase of efficiency. The lowest dose of 3×10^9 VP revealed an efficiency of at least 97 % eGFP⁺ rMSC

(Fig. 1a). Increasing virus titers led to a dose-dependent increase of the mean fluorescence intensity (MFI) (Fig. 1b). Fluorescence microscopy studies showed strong and dose-dependent fluorescence intensity. Untransduced controls showed no fluorescence. Brightfield images revealed no morphologic abnormalities of eGFP⁺ cells when compared with eGFP⁻ controls (Fig. 1c).

Metabolism quantified by XTT test showed that different eGFP virus doses resulted in a dose-dependent, minimally reduced absorbance $(2.14\pm0.03,\ 2.14\pm0.03,\ 2.13\pm0.02,\ 2.10\pm0.02,\ respectively,\ p<0.05,\ each)$ compared with untransduced controls (2.20 ± 0.04) (Fig. 2a). No significant differences were detected for caspase-3/-7 measurements compared with untransduced controls $(p\geq0.05,\ each)$. The

positive control, 1 mg/ml of 5 μ M camptothecin-treated cells, revealed a significant increase of caspase activity (p < 0.05, each) (Fig. 2b).

For subsequent labeling experiments with ferucarbotran, cells were transduced with a titer of 3×10^9 VP, due to excellent transduction efficiency with the lowest toxicity.

Cell Labeling with Ferucarbotran

eGFP⁺ rMSC were labeled with ferucarbotran at concentrations of 12.5, 25, 50, or 100 μ g Fe/ml. In comparison with unlabeled controls (2.02 \pm 0.02), there was a significant, but minimal (2.3 %), increase in cell metabolism within cells

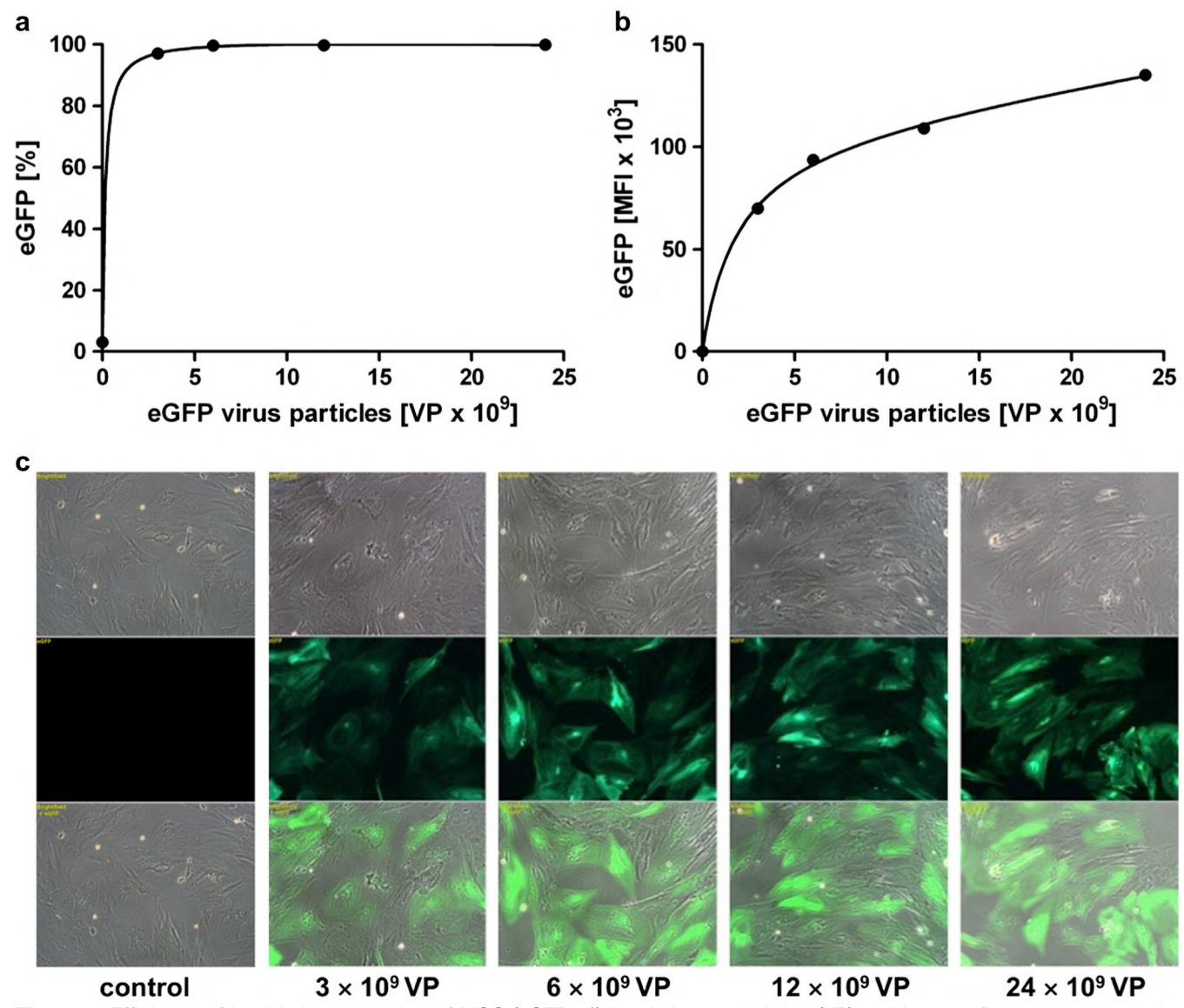


Fig. 1. a Efficiency of lentiviral transduction of MSC (eGFP %) in relation to viral titer (VP) and **b** mean fluorescence intensity (MFI). Note the dose-dependent increase of efficiency and MFI with an efficiency of at least 97 %. **c** Representative brightfield (top), corresponding fluorescence micrographs (middle), and merges (bottom) for different virus titers (magnification × 100). Images show strong and dose-dependent fluorescence of eGFP⁺ MSC.

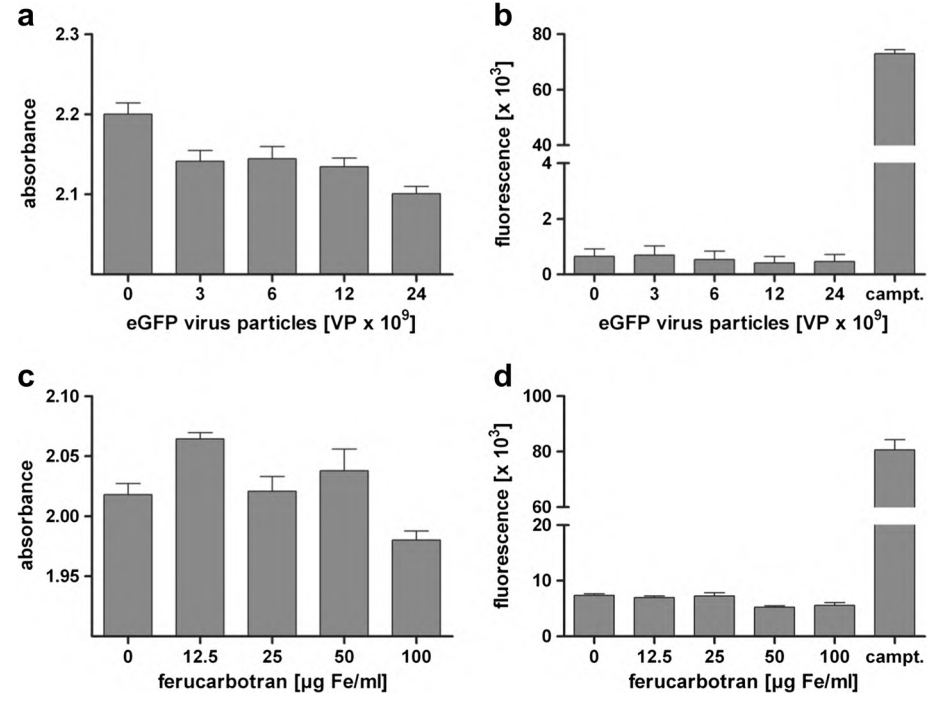


Fig. 2. XTT-test and caspase-3/-7 measurements of different virus doses (a, b) and different ferucarbotran concentrations (c, d). Transduced or labeled samples showed a minimal influence in cell viability (a, c) while no induction of apoptosis was observed (b, d).

transduced with 12.5 μ g Fe/ml (2.06 \pm 0.01, p = 0.02). In contrary, 25 and 50 μ g Fe/ml showed no significant differences in metabolism (2.02 \pm 0.02, p = 0.85; 2.04 \pm 0.03, p = 0.41). The highest labeling concentration used (100 μ g Fe/ml) led to a significant, but minimal (1.9 %), decrease in metabolism (1.98 \pm 0.1, p = 0.04) (Fig. 2c).

No induction of apoptosis was observed with any concentration of ferucarbotran tested, while all samples were significantly different to the apoptotic positive control, camptothecin (p < 0.05, each) (Fig. 2d).

Iron Uptake

IDMS demonstrated a significant iron uptake at all ferucarbotran concentrations compared with unlabeled controls (p < 0.05) (Fig. 3a). Dose dependently, the iron uptake doubled significantly (p < 0.05) with increasing labeling concentrations (12.5, 25, and 50 µg Fe/ml) (3.3 ± 0.2, 5.0 ± 0.5, and 10.0 ± 1.0 pg Fe/cell; p < 0.05, each). eGFP⁺ rMSC labeled with 100 µg Fe/ml ferucarbotran, however, displayed a 5.5-fold increase (56.5 ± 5.5 pg Fe/cell, p = 0.004) compared with 50 µg Fe/ml labeling concentration.

These results were confirmed by Prussian blue staining. It showed a marked intracellular iron uptake in labeled rMSC at 24 h after labeling. Unlabeled cells revealed no staining (Fig. 3b). Cells labeled with low ferucarbotran concentration showed very little blue cytoplasmatic inclusions while cells labeled with 100 µg Fe/ml resulted in a high number of blue inclusions (Fig. 3c).

Chondrogenic Differentiation

Neither different virus doses of eGFP nor different ferucarbotran concentrations significantly reduced the synthesis of GAG ($p \ge 0.05$, each) in differentiated rMSC (Fig. 4a, c). After lentiviral transduction, the DNA content decreased dose dependently, but not significantly, in chondrogenic micromass cultures compared with untransduced controls ($p \ge 0.05$, each) (Fig. 4b). When normalized to DNA content, this results in an apparent increase in GAG accumulation. No statistically significant ($p \ge 0.05$, each) alterations in DNA content were observed when different ferucarbotran doses were tested (Fig. 4d).

MR Imaging

Compared with unlabeled controls, ferucarbotran-labeled eGFP⁺ rMSC showed a strong contrast on all MR pulse sequences and a significant decrease in T2 signal for higher labeling concentrations (50 and 100 μ g Fe/ml; p = 0.006 and p < 0.001) (Fig. 5a). These results were consistent with the dose-dependent increase of the intracellular iron content (Fig. 3a). In addition, rMSC labeled with ferucarbotran at a concentration of 100 μ g Fe/ml showed shorter T2 relaxation times compared with the other labeling concentrations (p < 0.05, each).

After chondrogenic differentiation, T2*-weighted MR images of the differentiated pellets revealed a dose-

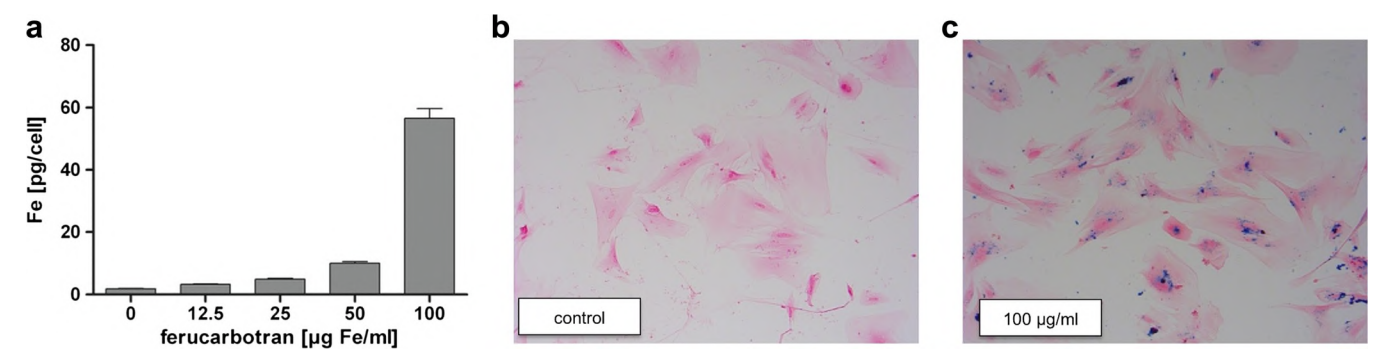


Fig. 3. a Quantification of intracellular iron (Fe) uptake by IDMS which demonstrated a significant, dose-dependent doubling of intracellular iron uptake (pg Fe/cell) for concentrations of 12.5–50 μ g Fe/ml while 100 μ g Fe/ml displayed a 5.5-fold increase (p = 0.004). Light microscopy of **b** unlabeled control and **c** labeled eGFP⁺ MSC (100 μ g Fe/ml) after Prussian blue staining (magnification \times 100). Multiple small blue cytoplasmic, perinuclear inclusions in almost all labeled MSC, indicating intracellular iron uptake, are shown.

dependent, marked signal loss of labeled rMSC compared with unlabeled controls (Fig. 5b (bottom)). The area of signal loss exceeded the size of the labeled pellets. These findings were in accordance with the macroscopic aspect of the differentiated pellet which showed a dose-dependent, brown staining of the chondrogenic cell pellets indicating iron uptake (Fig. 5b (top)).

The knee joint of the pig (Fig. 6a) reveals a detailed depiction of the anatomic landmark, and in particular, the cartilage while in the rat's knee (Fig. 6c) the cartilage is

hardly detectable. The rabbit knee (Fig. 6b) shows sufficient anatomic detail. Additionally, unlabeled and bifunctionally labeled rMSCs were implanted in fibrin clots in osteochondral defects in rabbit knees (Fig. 6d–f). Both defects were filled with a fibrin cell clot with 200,000 rMSCs each. The proximal defect contains unlabeled (white arrow) and the distal defect bifunctionally labeled (100 μ g/ml ferucarbotran) rMSCs (blue arrow). The knees were imaged by 7 T MRI using T1-, T2-, and T2*-weighted pulse sequences. T2* maps were calculated (Fig. 6f). MR imaging

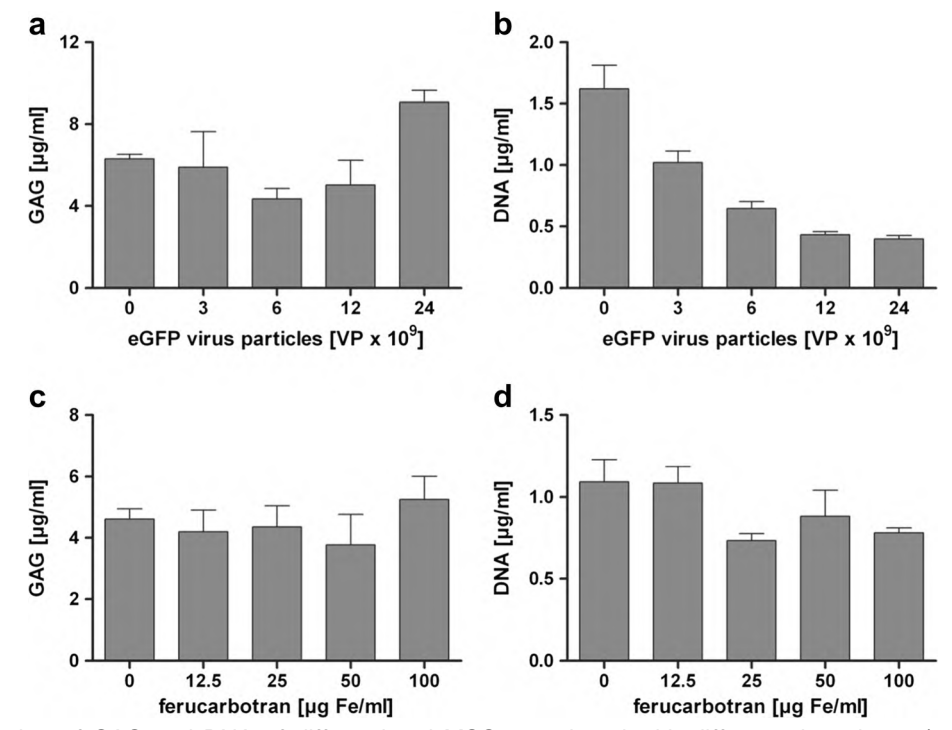


Fig. 4. Quantification of GAG and DNA of differentiated MSC transduced with different virus doses (\mathbf{a} , \mathbf{b}) or labeled with different ferucarbotran concentrations (\mathbf{c} , \mathbf{d}). No significant differences compared with controls were detected ($p \ge 0.05$, each). DNA content of cells transduced with \mathbf{b} different eGFP virus doses revealed a decrease of DNA content ($p \ge 0.05$, each) while \mathbf{d} increasing ferucarbotran concentrations did not result in any significant differences in DNA synthesis ($p \ge 0.05$, each).

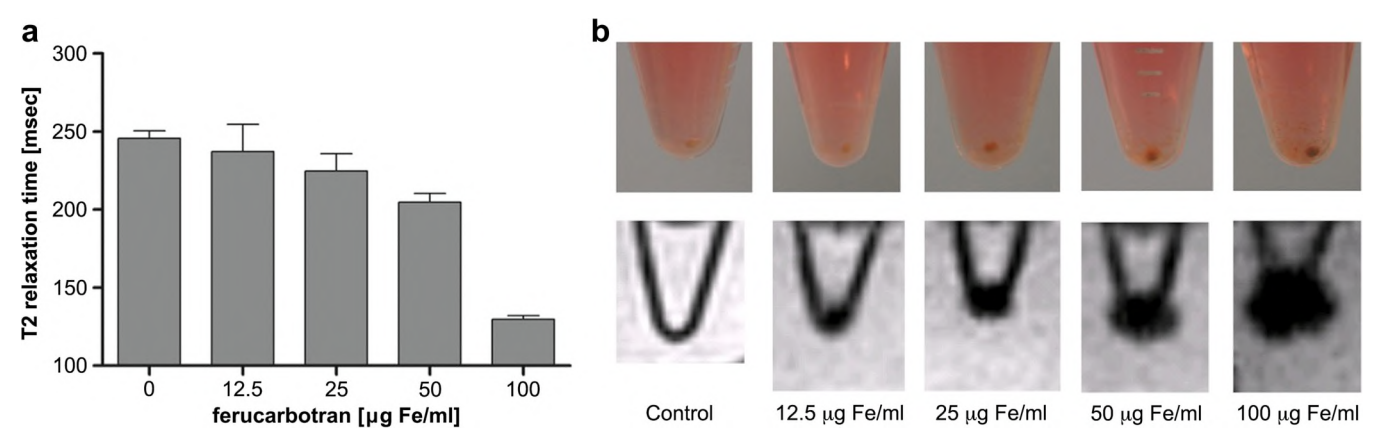


Fig. 5. a T2 relaxation rates of undifferentiated labeled MSC revealed a significant decrease at 50 and 100 μg Fe/ml compared with unlabeled controls. b Macroscopically, brown staining of differentiated cells (with macroscopic pellet formation) was consistent with a dose-dependent, marked signal loss in T2*-weighted MR images.

at 7 T showed a strong enhancement of contrast-to-noise ratio and anatomical details while, in contrast, control fibrin clots containing unlabeled cells did not reveal any significant contrast compared with healthy cartilage tissue. The labeled fibrin cell clot (blue arrow) in (Fig. 6e) demonstrated a pronounced hypointensity at the rim of the implant. The 7 T MRI images reveal sufficient discrimination between cartilage and subchondral bone and allow for good recognition of anatomical landmarks.

Discussion

MR imaging is currently considered the gold standard of noninvasive imaging methods for structural evaluation of cartilage lesions and repair in clinical routine. It offers a standardized and high-quality longitudinal imaging modality to assess the structure of cartilage, subchondral bone, and adjacent tissue [33, 34]. After chondrocyte or mesenchymal stem cell transplantation in articular cartilage defects, the monitoring of implanted cells and their development into cartilage (repair) tissue is currently of great scientific interest. Several studies have been conducted to evaluate the correlation between MRI findings and clinical outcome [35–37]. However, strong evidence to determine whether morphological MR imaging is reliable in predicting clinical outcome after cartilage repair is lacking [38]. The introduction of cellular MRI allows for noninvasive cell tracking in experimental models and might allow for the detection of early treatment failure [12, 14, 15]. It is an excellent tool for high-resolution visualization of the fate of cells after transplantation and for evaluation of therapeutic strategies [18]. Therefore, further preclinical studies are necessary to bridge the translational gap between basic research and the clinic.

Detection and tracking of implanted MSC *in vivo via* MR imaging require cell labeling with a contrast agent because MR imaging cannot distinguish unlabeled transplanted stem cells from host tissue.

The negatively charged iron oxide ferucarbotran (Resovist®) was FDA-approved for clinical applications in Europe and has already successfully been used for cell labeling of human MSC [22, 26, 27]. After labeling with ferucarbotran, a strong MR contrast effect was achieved without any need for additional transfection agents [22, 25, 27]. Compared with other iron-based contrast agents, ferucarbotran reveals some advantages such as a higher labeling efficiency for non-phagocytic and phagocytic cells without toxic side effects at appropriate concentrations [24–26].

To distinguish the implanted rMSC from native, unimplanted rMSC, a second intervention of the cellular, biochemical composition, was performed by transducing the rMSC with eGFP. This bifunctional labeling enables detection of the transduced, eGFP+ cells by fluorescence microscopy. Thereby, additional arthroscopic optical imaging investigations or immunohistological correlations of imaging findings are facilitated [39]. The fluorescent nature of eGFP+ cells provides a marker of cell origin, because the cell population can be easily identified and sorted [40]. We used an integrating viral vector system to allow for longterm observation. This might result in gene disruption and/or dysregulation, thus influencing proliferation as well as differentiation potential. Likewise, the over-expression of reporter gene might result in metabolic changes. In order to achieve high labeling efficiency while avoiding detrimental side effects, we analyzed various virus titers. Only a minimal, dose-dependent decrease in metabolic activity compared with untransduced controls was detected while apoptotic behavior was not affected by any means.

Our data showed a significant, but minimal increase in cell metabolism within cells labeled with 12 µg Fe/ml. This finding might be explained by iron being considered an innate and essential element in a number of cellular functions including metabolic processes [32, 41]. The intracellular incorporation of such a minimal amount of iron into normal iron metabolism might stimulate cell metabolism and thus lead to the described increase. On the other side, it has been described that iron oxides

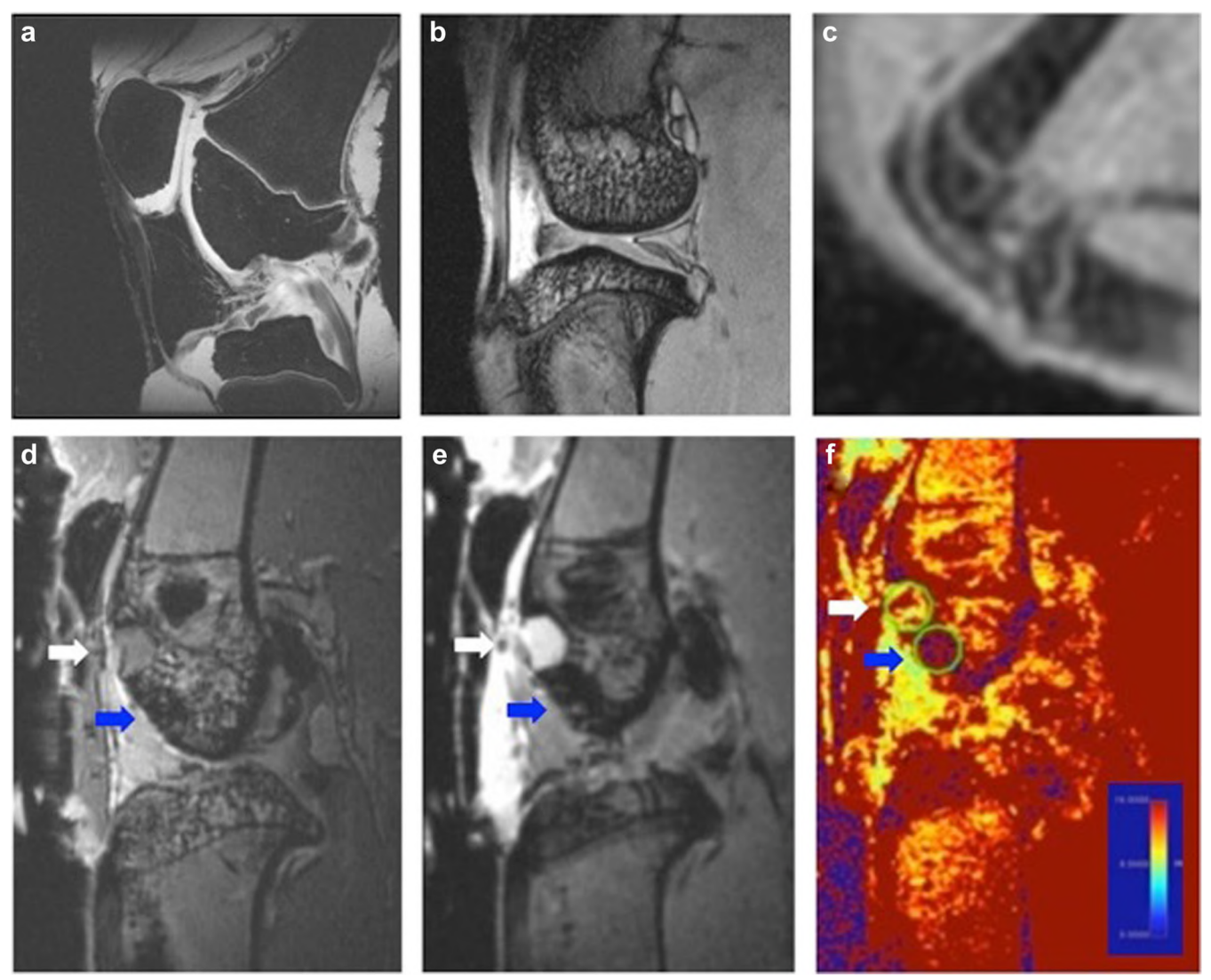


Fig. 6. MR images (sagittal view) of **a** a pig knee at 3 T, **b** rabbit knee at 1.5 T, and **c** rat knee at 3 T. The lower row (**d**–**f**) presents MR imaging of a rabbit knee with two surgically created osteochondral defects in the trochlea femoris. The proximal defect contains a fibrin cell clot with 200,000 unlabeled (white arrow) and the distal defect with 200,000 bifunctionally labeled (100 μg/ml ferucarbotran) rMSCs (blue arrow). The knee was imaged with different MRI sequences. **d** T1-weighted flash 3D. **e** T2*-weighted 3D. **f** Multi-gradient echo resulting in T2* maps.

can impair the viability of stem cells when they are internalized in too high quantities [25, 42]. In our data, we found a minimal, but significant, decrease in cell metabolism within cells labeled with ferucarbotran at a concentration of $100~\mu g$ Fe/ml. It is well known that an overload of cellular iron poses risks such as oxidative stress and the formation of reactive oxygen species and thereby, influences cell metabolism [43]. At concentrations lower than $100~\mu g$ Fe/ml, metabolism was not reduced. Therefore, we consider $50~\mu g$ Fe/ml to be the ideal labeling concentration in the described experimental setting.

For any cell labeling protocol with MSC and effective stem cell therapy, it is a prerequisite that—besides unimpaired cell viability—chondrogenic differentiation is not reduced by any means. In literature, conflicting data on the influence of SPIO labeling of mesenchymal stem cells on chondrogenic differentiation capacity exists. Some studies reported no influence on human bone marrow–derived MSC [44, 45], while other study groups demonstrated a negative effect [26, 46]. It has been described that higher labeling concentrations of >50 µg/ml have led to an impaired differentiation into chondrocytes [26, 47]. Therefore, we tested different ferucarbotran concentrations ranging from 12.5 to 100 µg/ml iron doses to rule out any dose-dependent effects in rMSC. The data showed a stable, macroscopic pellet formation indicating the chondrogenic differentiation of the cells. Interestingly, in the presented animal model, no impairment of differentiation capacity even at 100 µg/ml with an intracellular iron content of 56.5 pg Fe/cell was detected. Comparing these findings to Henning et al. [26], the intracellular iron uptake was much higher in rabbit

MSCs than in human MSCs. A possible explanation could be found in the different cell model used and might suggest that rabbit MSCs can endure comparably high intracellular iron concentrations without showing any apoptotic behavior at the same time.

There is a trend towards decreasing DNA content with increasing eGFP virus doses without being statistically significant. This might indicate long-term toxicity at higher virus doses, which leads to a retarded growth under chondrogenic differentiation conditions. This may have resulted in an apparent increase in GAG accumulation at higher virus doses when normalized to DNA content. Although the caspase activity directly after eGFP transduction did not reveal any impairment, the slight, but statistically significant, dose-dependent decrease of cell metabolism might give a first hint that higher virus doses or eGFP expression do not affect cell viability and DNA synthesis. Therefore, we suggest an application of $3-6 \times 10^9$ virus particles for further labeling procedures.

In the last years, several experimental in vivo models have been proposed to provide the researchers with further information that might help to understand underlying processes during cartilage repair procedures. Especially, small animal models (e.g., mouse or rat) exist, which allow for a high number of cases due to relatively low costs and simple logistics. However, the knee joint is too small and the cartilage thickness of the femoral condyle is too thin (mouse 0.058 mm [48]; rat 0.072 mm [48]) to serve as a good model for any (chondral or osteochondral) surgical cartilage repair technique. Moreover, small animals might be insufficient for the morphological depiction of pathologic detail or treatment effects in MR imaging even when used in dedicated small animal scanners. Larger animal models offer thicker cartilage: e.g., goats or pigs can be used to depict these details better (goat 0.7–1.5 mm [49]; pigs up to 1.5 mm [50]). These dimensions are similar to the conditions found in the human knee joint (1.69–2.55 mm [51]), and therefore, the translation might be easier. But large animals are expensive and often logistically impractical so that a significant number in a treatment group is difficult to achieve.

Our intermediate-sized animal model in rabbits (cartilage thickness 0.21–0.46 mm [49]) in this study is a reasonable compromise. It enables precise surgery while being financially and logistically affordable. The proof of principle imaging data offers a high resolution and morphological depiction of articular cartilage. Compared with the smaller rat model, the quality of information of the anatomy available for the researcher is significantly enhanced. Cartilage imaging highly depends on the quality of the image itself [52]. In our study, MRI performed at 7 T field strength led to sufficient discrimination between cartilage and subchondral bone and allowed for good recognition of anatomical landmarks. Fat suppression eliminates artifacts that can be superimposed to the cartilage-bone interface. Thereby, the contrast of the image at this interface is

improved and a better depiction of the cartilage boundaries can be achieved [53].

However, there is some hypointensity at the rim of the implant, which can be detected in both labeled and unlabeled implants. Primarily, this might be caused by compacting of cancellous bone at the rim during drilling of the artificial osteochondral defects. Another explanation might be found in the implant itself. After preparation of the fibrin cell clot, we controlled the successful incorporation of the labeled cells by fluorescence microscopy. Due to the additional, bifunctional transduction of all rMSCs with eGFP, the cell distribution could be easily visualized. Generally, an even cell distribution was initially achieved within the clots. However, during the further precipitation of the fibrin cell clot, some cells might migrate to the rim of the clot and, therefore, will result in a pronounced hypointensity in MR imaging at the rim while simultaneously, compared with the unlabeled clot, the entire clot is still hypointense due to the remaining distributed cells (Fig. 6d-f). Lo et al. demonstrated that changes in tissue rigidity could play an important role in cell locomotion [54]. They showed that fibroblasts preferentially migrate from a soft to hard surface. Additionally, Duong et al. stated that cells adhere to the stiffness of the surface of fibrin matrices [55]. The fibrin cell clot is hardened from rim to center. This might be an explanation for this cell condensation and hypointensity at the rim in this early phase of clot implantation.

The presented rabbit model also demonstrates the feasibility of acquiring cartilage T2* maps in the rabbit knees for a better delineation of the tissue containing labeled cells. Our rabbit model combines the advantages of small and large animal models by enabling precise surgery and high-resolution MR imaging while being financially and logistically affordable.

Several limitations pertain to this study. Imaging was performed with cadaveric knee joints and not in a living animal. Therefore, follow-up analyses of the implanted cells were not possible. Future work will aim at the visualization of labeled cell clots at later time points, with the ultimate aim of monitoring complete integration into surrounding tissue by MRI. Currently, ferucarbotran is not distributed any more in Europe or North America. We used it for this proof of principle study because its properties have been extensively studied in the literature and its imaging characteristics are comparable with other contrast agents as, *e.g.*, ferumoxides (Feridex IV, Berlex Laboratories; and Endorem, Guebert). Thus, our results are easily translatable to other contrasts models [56, 57].

Conclusions

In conclusion, rMSC were lentivirally transduced to express eGFP and magnetically labeled with the iron oxide contrast agent ferucarbotran without adverse effects on cellular viability or chondrogenic differentiation capacity. With histological staining, mass spectrometry, and MR imaging,

it was possible to accurately determine or visualize intracellular iron uptake in ferucarbotran-labeled rMSC. The strong contrast of labeled cells on MR and fluorescent images might allow for *in vivo* stem cell tracking with immunohistological correlation in an intermediate-sized but still practical animal model, which improves image quality over existing small animal models for a better depiction of anatomic and pathologic details.

Acknowledgments. We thank M. Settles for his support in MRI imaging and G. Piontek for Prussian Blue staining.

Funding Information. This work was supported by the German Research Foundation through DFG grant HE 4578/3-1.

Compliance with Ethical Standards

Conflict of Interest

The authors declare that they have no conflict of interest.

References

- Yong KW, Choi JR, Mohammadi M et al (2018) Mesenchymal stem cell therapy for ischemic tissues. Stem Cells Int 2018:8179075
- Shafei AE, Ali MA, Ghanem HG, et al. (2017) Mesenchymal stem cell therapy: A promising cell-based therapy for treatment of myocardial infarction. J Gene Med 19:e2995
- Kakkar A, Sorout A, Tiwari M, Shrivastava P, Meena P, Saraswat SK, Srivastava S, Datt R, Pandey S (2018) Current status of stem cell treatment for type I diabetes mellitus. Tissue Eng Regen Med 15:699– 709
- Scuteri A, Monfrini M (2018) Mesenchymal Stem Cells as New Therapeutic Approach for Diabetes and Pancreatic Disorders. Int J Mol Sci 19:2783
- Gardner OF, Archer CW, Alini M et al (2013) Chondrogenesis of mesenchymal stem cells for cartilage tissue engineering. Histol Histopathol 28:23–42
- Centeno CJ, Busse D, Kisiday J et al (2008) Increased knee cartilage volume in degenerative joint disease using percutaneously implanted, autologous mesenchymal stem cells. Pain Physician 11:343–353
- Goldberg A, Mitchell K, Soans J, Kim L, Zaidi R (2017) The use of mesenchymal stem cells for cartilage repair and regeneration: a systematic review. J Orthop Surg Res 12:39
- Peterson L, Vasiliadis HS, Brittberg M, Lindahl A (2010) Autologous chondrocyte implantation: a long-term follow-up. Am J Sports Med 38:1117–1124
- Jorgensen C, Gordeladze J, Noel D (2004) Tissue engineering through autologous mesenchymal stem cells. Curr Opin Biotechnol 15:406– 410
- Chen FH, Tuan RS (2008) Mesenchymal stem cells in arthritic diseases. Arthritis Res Ther 10:223
- Murphy JM, Fink DJ, Hunziker EB, Barry FP (2003) Stem cell therapy in a caprine model of osteoarthritis. Arthritis Rheum 48:3464– 3474
- Jing XH, Yang L, Duan XJ, Xie B, Chen W, Li Z, Tan HB (2008) In vivo MR imaging tracking of magnetic iron oxide nanoparticle labeled, engineered, autologous bone marrow mesenchymal stem cells following intra-articular injection. Joint Bone Spine 75:432–438
- van Velthoven CT, Kavelaars A, Heijnen CJ (2012) Mesenchymal stem cells as a treatment for neonatal ischemic brain damage. Pediatr Res 71:474–481
- Henning TD, Gawande R, Khurana A, et al. (2012) Magnetic resonance imaging of ferumoxide-labeled mesenchymal stem cells in cartilage defects: in vitro and in vivo investigations. Mol Imaging 11:107-200
- Hwang YH, Lee DY (2012) Magnetic resonance imaging using heparin-coated superparamagnetic iron oxide nanoparticles for cell tracking in vivo. Quant Imaging Med Surg 2:118–123

- Jaffer FA, Weissleder R (2005) Molecular imaging in the clinical arena. Jama 293:855–862
- Ding W, Bai J, Zhang J, Chen Y, Cao L, He Y, Shen L, Wang F, Tian J (2004) In vivo tracking of implanted stem cells using radio-labeled transferrin scintigraphy. Nucl Med Biol 31:719–725
- Jasmin, Torres AL, Jelicks L et al (2012) Labeling stem cells with superparamagnetic iron oxide nanoparticles: analysis of the labeling efficacy by microscopy and magnetic resonance imaging. Methods Mol Biol 906:239–252
- Bulte JW, Kraitchman DL (2004) Iron oxide MR contrast agents for molecular and cellular imaging. NMR Biomed 17:484

 499
- Meier R, Henning TD, Boddington S, Tavri S, Arora S, Piontek G, Rudelius M, Corot C, Daldrup-Link HE (2010) Breast cancers: MR imaging of folate-receptor expression with the folate-specific nanoparticle P1133. Radiology 255:527–535
- Lalande C, Miraux S, Derkaoui SM et al (2011) Magnetic resonance imaging tracking of human adipose derived stromal cells within threedimensional scaffolds for bone tissue engineering. Eur Cell Mater 21:341–354
- Henning TD, Wendland MF, Golovko D, Sutton EJ, Sennino B, Malek F, Bauer JS, McDonald DM, Daldrup-Link H (2009) Relaxation effects of ferucarbotran-labeled mesenchymal stem cells at 1.5T and 3T: discrimination of viable from lysed cells. Magn Reson Med 62:325–332
- Reimer P, Balzer T (2003) Ferucarbotran (Resovist): a new clinically approved RES-specific contrast agent for contrast-enhanced MRI of the liver: properties, clinical development, and applications. Eur Radiol 13:1266–1276
- Boutry S, Brunin S, Mahieu I, Laurent S, Elst LV, Muller RN (2008) Magnetic labeling of non-phagocytic adherent cells with iron oxide nanoparticles: a comprehensive study. Contrast Media Mol Imaging 3:223–232
- Metz S, Bonaterra G, Rudelius M, Settles M, Rummeny EJ, Daldrup-Link HE (2004) Capacity of human monocytes to phagocytose approved iron oxide MR contrast agents in vitro. Eur Radiol 14:1851–1858
- Henning TD, Sutton EJ, Kim A, Golovko D, Horvai A, Ackerman L, Sennino B, McDonald D, Lotz J, Daldrup-Link HE (2009) The influence of ferucarbotran on the chondrogenesis of human mesenchymal stem cells. Contrast Media Mol Imaging 4:165–173
- Mailander V, Lorenz MR, Holzapfel V et al (2008) Carboxylated superparamagnetic iron oxide particles label cells intracellularly without transfection agents. Mol Imaging Biol 10:138–146
- Daldrup-Link HE, Rudelius M, Piontek G, Metz S, Bräuer R, Debus G, Corot C, Schlegel J, Link TM, Peschel C, Rummeny EJ, Oostendorp RAJ (2005) Migration of iron oxide-labeled human hematopoietic progenitor cells in a mouse model: in vivo monitoring with 1.5-T MR imaging equipment. Radiology 234:197–205
- Henning TD, Gawande R, Khurana A, Tavri S, Mandrussow L, Golovko D, Horvai A, Sennino B, McDonald D, Meier R, Wendland M, Derugin N, Link TM, Daldrup-Link HE (2012) Magnetic resonance imaging of ferumoxide-labeled mesenchymal stem cells in cartilage defects: in vitro and in vivo investigations. Mol Imaging 11:197–209
- Ma GS, Qi CM, Liu NF, Shen CX, Chen Z, Liu XJ, Hu YP, Zhang XL, Teng GJ, Ju SH, Ma M, Tang YL (2011) Efficiently tracking of stem cells in vivo using different kinds of superparamagnetic iron oxide in swine with myocardial infarction. Chin Med J 124:1199–1204
- Schrauth JH, Lykowsky G, Hemberger K et al (2016) Comparison of multiple quantitative MRI parameters for characterization of the goat cartilage in an ongoing osteoarthritis: dGEMRIC, T1rho and sodium. Z Med Phys 26:270–282
- Nejadnik H, Henning TD, Castaneda RT, Boddington S, Taubert S, Jha P, Tavri S, Golovko D, Ackerman L, Meier R, Daldrup-Link HE (2012) Somatic differentiation and MR imaging of magnetically labeled human embryonic stem cells. Cell Transplant 21:2555–2567
- Domayer SE, Welsch GH, Dorotka R, Mamisch T, Marlovits S, Szomolanyi P, Trattnig S (2008) MRI monitoring of cartilage repair in the knee: a review. Semin Musculoskelet Radiol 12:302–317
- 34. Crema MD, Roemer FW, Marra MD, Burstein D, Gold GE, Eckstein F, Baum T, Mosher TJ, Carrino JA, Guermazi A (2011) Articular cartilage in the knee: current MR imaging techniques and applications in clinical practice and research. Radiographics 31:37–61

- Tins BJ, McCall IW, Takahashi T et al (2005) Autologous chondrocyte implantation in knee joint: MR imaging and histologic features at 1-year follow-up. Radiology 234:501–508
- Takahashi T, Tins B, McCall IW et al (2006) MR appearance of autologous chondrocyte implantation in the knee: correlation with the knee features and clinical outcome. Skelet Radiol 35:16–26
- Henderson IJ, Tuy B, Connell D et al (2003) Prospective clinical study of autologous chondrocyte implantation and correlation with MRI at three and 12 months. J Bone Joint Surg (Br) 85:1060–1066
- de Windt TS, Welsch GH, Brittberg M, et al. (2013) Is magnetic resonance imaging reliable in predicting clinical outcome after articular cartilage repair of the knee? A systematic review and metaanalysis. Am J Sports Med 41:1695–1702
- Mina M, Braut A (2004) New insight into progenitor/stem cells in dental pulp using Collal-GFP transgenes. Cells Tissues Organs 176:120–133
- Balic A, Rodgers B, Mina M (2009) Mineralization and expression of Colla1-3.6GFP transgene in primary dental pulp culture. Cells Tissues Organs 189:163–168
- Richardson DR, Chua AC, Baker E (1999) Activation of an iron uptake mechanism from transferrin in hepatocytes by small-molecularweight iron complexes: implications for the pathogenesis of ironoverload disease. J Lab Clin Med 133:144–151
- Daldrup-Link HE, Rudelius M, Oostendorp RA et al (2003) Targeting of hematopoietic progenitor cells with MR contrast agents. Radiology 228:760–767
- Hoepken HH, Korten T, Robinson SR, Dringen R (2004) Iron accumulation, iron-mediated toxicity and altered levels of ferritin and transferrin receptor in cultured astrocytes during incubation with ferric ammonium citrate. J Neurochem 88:1194–1202
- Pawelczyk E, Arbab AS, Pandit S, Hu E, Frank JA (2006) Expression of transferrin receptor and ferritin following ferumoxides-protamine sulfate labeling of cells: implications for cellular magnetic resonance imaging. NMR Biomed 19:581–592
- Arbab AS, Yocum GT, Rad AM, Khakoo AY, Fellowes V, Read EJ, Frank JA (2005) Labeling of cells with ferumoxides-protamine sulfate complexes does not inhibit function or differentiation capacity of hematopoietic or mesenchymal stem cells. NMR Biomed 18:553–559
- Kostura L, Kraitchman DL, Mackay AM, Pittenger MF, Bulte JWM (2004) Feridex labeling of mesenchymal stem cells inhibits chondrogenesis but not adipogenesis or osteogenesis. NMR Biomed 17:513

 517

- Bulte JW, Kraitchman DL, Mackay AM, Pittenger MF (2004) Chondrogenic differentiation of mesenchymal stem cells is inhibited after magnetic labeling with ferumoxides. Blood 104:3410–3412 author reply 3412-3413
- Stockwell RA (1971) The interrelationship of cell density and cartilage thickness in mammalian articular cartilage. J Anat 109:411–421
- 49. Frisbie DD, Cross MW, McIlwraith CW (2006) A comparative study of articular cartilage thickness in the stifle of animal species used in human pre-clinical studies compared to articular cartilage thickness in the human knee. Vet Comp Orthop Traumatol 19:142–146
- Chu CR, Szczodry M, Bruno S (2010) Animal models for cartilage regeneration and repair. Tissue Eng Part B Rev 16:105–115
- Shepherd DE, Seedhom BB (1999) Thickness of human articular cartilage in joints of the lower limb. Ann Rheum Dis 58:27–34
- Kshirsagar AA, Watson PJ, Tyler JA et al (1998) Measurement of localized cartilage volume and thickness of human knee joints by computer analysis of three-dimensional magnetic resonance images. Investig Radiol 33:289–299
- Peterfy CG, van Dijke CF, Janzen DL, Glüer CC, Namba R, Majumdar S, Lang P, Genant HK (1994) Quantification of articular cartilage in the knee with pulsed saturation transfer subtraction and fat-suppressed MR imaging: optimization and validation. Radiology 192:485–491
- Lo CM, Wang HB, Dembo M, Wang YL (2000) Cell movement is guided by the rigidity of the substrate. Biophys J 79:144–152
- Duong H, Wu B, Tawil B (2009) Modulation of 3D fibrin matrix stiffness by intrinsic fibrinogen-thrombin compositions and by extrinsic cellular activity. Tissue Eng Part A 15:1865–1876
- Wang YX (2011) Superparamagnetic iron oxide based MRI contrast agents: current status of clinical application. Quant Imaging Med Surg 1:35–40
- Xiao YD, Paudel R, Liu J, Ma C, Zhang ZS, Zhou SK (2016) MRI contrast agents: classification and application (review). Int J Mol Med 38:1319–1326